Rapidly reversible redox transformation in nanophase manganese oxides at room temperature triggered by changes in hydration

Nancy Birkner and Alexandra Navrotsky[1]

Peter A. Rock Thermochemistry Laboratory and Nanomaterials in the Environment, Agriculture, and Technology Organized Research Unit, University of California, Davis, CA 95616

Contributed by Alexandra Navrotsky, March 24, 2014 (sent for review October 23, 2013)

Chemisorption of water onto anhydrous nanophase manganese oxide surfaces promotes rapidly reversible redox phase changes as confirmed by calorimetry, X-ray diffraction, and titration for manganese average oxidation state. Surface reduction of bixbyite (Mn_2O_3) to hausmannite (Mn_3O_4) occurs in nanoparticles under conditions where no such reactions are seen or expected on grounds of bulk thermodynamics in coarse-grained materials. Additionally, transformation does not occur on nanosurfaces passivated by at least 2% coverage of what is likely an amorphous manganese oxide layer. The transformation is due to thermodynamic control arising from differences in surface energies of the two phases (Mn_2O_3 and Mn_3O_4) under wet and dry conditions. Such reversible and rapid transformation near room temperature may affect the behavior of manganese oxides in technological applications and in geologic and environmental settings.

phase transformation | oxidation/reduction | water adsorption/desorption

Manganese oxides are ubiquitous in the natural environment, often occurring as very fine grained (nanopahase) precipitates and coatings, and also find numerous technological applications, especially in catalysis. Easy variation of manganese oxidation state (Mn^{2+}, Mn^{3+}, Mn^{4+}) lends complexity to phase behavior and physical and chemical properties of manganese oxides. The thermodynamic stability of manganese oxide nanoparticles helps determine the robustness of such oxides and their behavior in soils and larger-scale geochemical cycles, as well as in applications in catalysis, renewable energy, and environmental remediation. The structure and energetics of nanoparticle surfaces are influenced by the phase present and its oxidation state and by the extent of surface hydration; thus dry surfaces are structurally and thermodynamically distinct from hydrated surfaces (1, 2). Using Mn_3O_4 (hausmannite), Mn_2O_3 (bixbyite), and MnO_2 (pyrolusite), previously, we showed that the position in temperature–oxygen fugacity space, of oxidation–reduction (redox) phase equilibria, is shifted at the nanoscale due to differences in nanophase surface energy as a function of particle size and surface hydration and that this thermodynamic shift is in favor of the lower surface energy phase (3). In the manganese oxides, the surface energy increases in the order hausmannite, bixbyite, pyrolusite, so small particle size favors the more reduced oxide phase.

This paper summarizes observations in the nanoscale Mn_2O_3–Mn_3O_4 system, which is found to undergo rapidly reversible redox phase transformations at room temperature induced by the adsorption/desorption of surface water. It is expected that the degree of reduction is a function of both average particle size and particle size distribution, but this work focuses on only one representative material to provide proof of concept. The rapid response of activated surfaces to changing hydration condition implies thermodynamic control and has implications for geochemistry, planetary science, and technology.

Results

A synthetic Mn_2O_3 powder was prepared by methods described previously (3). Its synthesis and characterization are documented in *SI Text*. The X-ray powder pattern (Fig. S1) shows the starting material is nanophase Mn_2O_3. Its specific surface area, determined by N_2 adsorption, is 18.54 ± 0.36 m^2/g (2941 m^2/mol). Using the assumption of spherical particle shape as well as the density of bixbyite (4.95 g/cm^3) to make the calculation, the measured specific surface area corresponds to an average particle size of 32 nm, which agrees well with X-ray diffraction (XRD) analysis. The water content was measured via thermogravimetry, which yielded a composition of Mn_2O_3-0.0359H_2O. After annealing at 700 °C, powder XRD confirmed that the phase remained Mn_2O_3. The manganese average oxidation state of initial and annealed Mn_2O_3 was found by iodometric titration to be 3.000 ± 0.002 and 3.000 ± 0.003, respectively, confirming each sample to be pure stoichiometric Mn_2O_3.

Heating the sample either in air or under vacuum at 350 °C (Fig. S2) or 700 °C (Fig. S3) did not produce any change in the phase; it remained pure bixbyite with the same average particle size. Although the water content diminished with heating, the bixbyite phase did not transform or coarsen. The sample was then subjected to various heating and hydration/dehydration regimens to induce possible redox phase transformation (Table 1 and Fig. 1).

Water adsorption at room temperature during calorimetric experiment (see *Materials and Methods* and *SI Text*) induced partial phase transformation of Mn_2O_3 to a mixture of 85% Mn_2O_3 and 15% Mn_3O_4 as measured by XRD for samples pretreated with the 700 °C procedure, which used a heating/cooling cycle of 25–350 °C at 10 °C/min, 350 °C for 4 h, 350–700 °C at 10 °C/min, 700–25 °C at 10 °C/min (Fig. 2). This experiment demonstrated a structural transformation associated with water chemisorption. In contrast, samples subjected to the 350 °C

Significance

In the present work, we find rapid and reversible transformations between nanoscale Mn_2O_3 (more oxidized) and Mn_3O_4 (more reduced) at room temperature as a function of changing hydration level. These phase transformations are controlled by a thermodynamic factor (difference in surface energy). Redox reactive Mn-oxide phases may be sensitive markers, on short time scales, of variations in water activity as well as oxygen fugacity in the local environment. Hydration-induced phase transformation has applications to geochemistry, planetary science, and technology.

Author contributions: N.B. and A.N. designed research; N.B. performed research; N.B. and A.N. analyzed data; and N.B. and A.N. wrote the paper.

The authors declare no conflict of interest.

[1]To whom correspondence should be addressed. E-mail: anavrotsky@ucdavis.edu.

This article contains supporting information online at www.pnas.org/lookup/suppl/doi:10.1073/pnas.1320014111/-/DCSupplemental.

Table 1. Comparison of heating methods and their effect on phases present

Heating*	Synthesized Mn_2O_3 and particle size (nm)†	Phase and particle size (nm)† after heat treatment	Mn average oxidation state after heat treatment	Surface water, mole H_2O per mole Mn_2O_3	Residual water, mole H_2O per mole Mn_2O_3	Phase and particle size (nm)† after water adsorption	Phase and particle size (nm)† after one large dose of H_2O	Phase and particle size (nm)† after water adsorption, followed by heating to desorb surface water (nm)†
700 °C	bixbyite (32.6)	bixbyite (33.0)	3.00 ± 0.01	0.0359	1.00E-5	85% Mn_2O_3 (28.7) and 15% Mn_3O_4 (25.6)	85% Mn_2O_3 (30.7) and 15% Mn_3O_4 (26.9)	bixbyite (31.0)
350 °C	bixbyite (32.6)	bixbyite (32.9)	3.00 ± 0.01	0.0348	1.12E-3	bixbyite (31.6)	bixbyite (31.5)	bixbyite (31.7)

*Final temperature at which the sample is outgassed under nitrogen, in preparation for water adsorption calorimetry.
†Particle size obtained using XRD and calculations using the Scherrer equation (40, 41). Considering the approximations used, we consider calculated particle sizes of all samples to be the same within probable uncertainties.

procedure, 25–350 °C at 10 °C/min, 350 °C for 4 h, 350–25 °C at 10 °C/min, did not show any detectable transformation (Table 2). There was no appreciable change in the average particle size of any of the samples. The reverse experiment (treatment of hausmannite by water vapor under similar conditions) was performed previously (3), and it was found that adsorption of water onto anhydrous Mn_3O_4 does not promote oxidation to Mn_2O_3 but to MnOOH, which may indicate that MnOOH is of lower surface energy than Mn_3O_4, as is the case for iron oxyhydroxides compared with hematite (2). Since Mn_3O_4 has a lower surface energy than Mn_2O_3, nanoscale Mn_3O_4 is thermodynamically stable to higher oxygen fugacity than is bulk Mn_3O_4. It might be possible to show that oxidation of hausmannite will not occur at temperature–oxygen fugacity conditions where it should occur for bulk Mn_3O_4, but that is a different experiment not done here. The chemical reaction for bixbyite (Mn_2O_3) transformation to hausmannite (Mn_3O_4) comes directly from their redox equilibria; thus oxidation consumes oxygen gas and reduction evolves it.

$$3Mn_2O_3 = 2Mn_3O_4 + 0.5O_2 \quad [1]$$

The differential enthalpy of adsorption is the measured enthalpy of water adsorption (and of any concomitant redox reaction or structural change) when a small dose of water is adsorbed. The integral enthalpy of adsorption and its associated water coverage is taken as the sum of differential enthalpies and adsorption amounts at the coverage where further water is only physically adsorbed, with an enthalpy of adsorption equal to the condensation enthalpy of water vapor at room temperature (−44 kJ/mol).

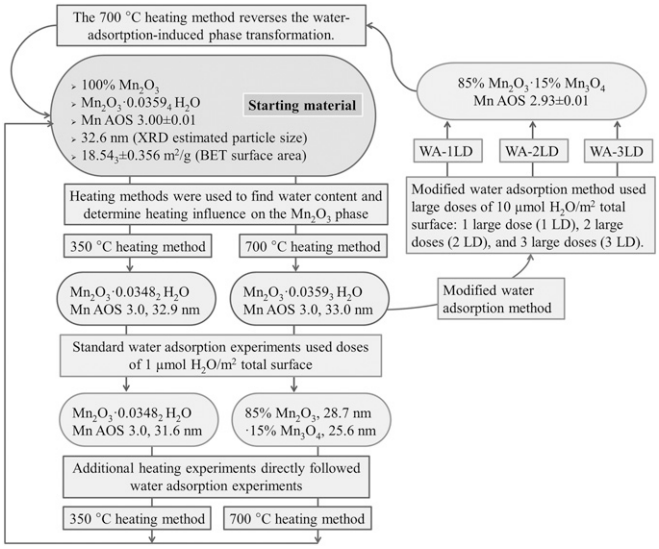

Fig. 1. Schematic summary of experiments that probe room-temperature water-adsorption-induced phase transformation.

Fig. 3 shows measured differential enthalpy of water adsorption as a function of coverage (method from ref. 4) for samples prepared at 350 °C and 700 °C. The most significant differential enthalpy differences occur during the first few doses in the experiment (Fig. 3, *Inset*).

The sample prepared at 350 °C showed no transformation to Mn_3O_4. A coverage of 4.8 H_2O/nm^2 with integral enthalpy of adsorption of −103.1 ± 0.9 kJ/mol was obtained, which compares well to the previously published value of 4.8 H_2O/nm^2 and integral enthalpy of adsorption of −103.5 kJ/mol (3). The manganese average oxidation state was 3.00 ± 0.01, confirming the absence of any reductive transformation.

In contrast, for samples pretreated by the 700 °C procedure, the integral enthalpy of water adsorption was −90.2 ± 0.9 kJ/mol, indicating water adsorption coupled with partial reduction of Mn_2O_3 to Mn_3O_4 involved an additional endothermic enthalpy characteristic of a reduction reaction that was concentrated in the first few doses of water. Manganese average oxidation state (see Table 2) obtained by titration, was 2.93 ± 0.01. This degree of oxidation state change is consistent with the reduction of 15% Mn_2O_3 (see *SI Text*).

It is interesting that only 15% reduction occurred. Although the reason for this is not fully understood, we surmise that the degree of reduction is related to the particle size distribution, with larger particles having less (or no) thermodynamic driving force for reduction. It is also possible that a reduced surface layer hinders further transformation and core-shell particles could be formed. We expect that the degree of reduction may vary among differently prepared samples.

In an additional water adsorption experiment, a sample that underwent water-adsorption-induced phase transformation was then exposed immediately afterward to the 700 °C procedure. XRD and manganese average oxidation state titration showed that the transformed mixture of 85% Mn_2O_3 and 15% Mn_3O_4 had transformed back to Mn_2O_3 on heating and associated dehydration. The lattice constants and particle size for this Mn_2O_3 phase (Fig. S4) were essentially unchanged from those of the initial Mn_2O_3 sample (Fig. S1 and Table 1).

The influence on phase transformation by variation of the size of the water dose was then examined. This set of experiments used the 700 °C procedure on a series of initial Mn_2O_3 samples followed by modified water adsorption calorimetry experiments (Fig. 1 and Table 2) in which the doses were increased from 1 µmol/m^2 total to 10 µmol/m^2 total sample surface. XRD identified similar phase transformation from Mn_2O_3 to a mixture of 85% Mn_2O_3 and 15% Mn_3O_4. The Mn average oxidation state was diminished from 3.00 to 2.93 ± 0.01. The crystallite size did not change significantly. Thus, there is little or no dependence of

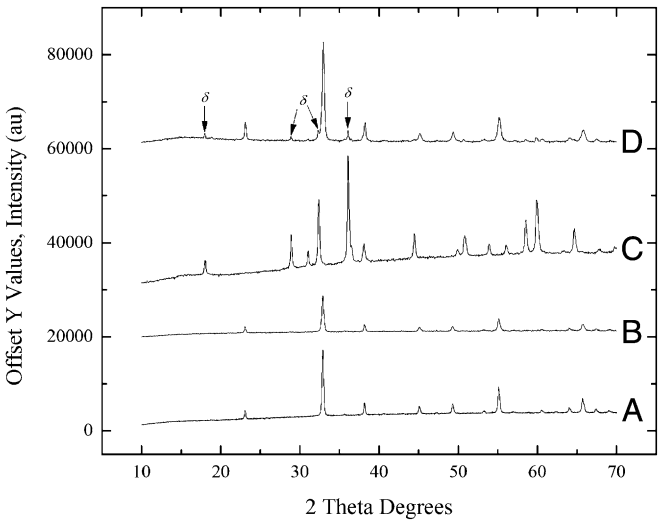

Fig. 2. X-ray powder pattern of (*A*) nanophase Mn_2O_3 prepared using the 700 °C procedure before water adsorption microcalorimetry, (*B*) nanophase Mn_2O_3 as reference comparison, (*C*) nanophase Mn_3O_4 as reference comparison, and (*D*) nanophase Mn_2O_3 sample after water-adsorption-induced partial phase transformation to Mn_3O_4.

the product on the size of individual water doses or the rate at which they are applied, providing the sample is first activated at 700 °C.

It is striking that the particles heat treated at lower temperatures (350 °C) did not undergo partial reduction upon exposure to water vapor at room temperature. The lower temperature samples had higher initial water content, with 2.3% surface coverage for the 350 °C sample compared with 0.002% for the 700 °C sample (Table 2). Another experiment was designed to probe the possible effect of such surface water on the reductive transformation. A sample of nanophase Mn_2O_3 was pretreated using the 700 °C procedure followed by a water adsorption experiment that dosed the dried sample with water vapor to coat ~2% of the total surface. Next, the sample was equilibrated for 24 h in the gas adsorption apparatus, after which, water adsorption calorimetry was resumed using the standard protocol (adding doses of 1 μmol H_2O/ m^2 total surface). The initial and final samples were pure Mn_2O_3 (Fig. S5) with no evidence of reduction. The integral enthalpy of water adsorption was −103.1 ± 0.9 kJ/mol, which is consistent with the absence of an endothermic contribution from reduction. This value corresponds well with earlier values (3) of water adsorption enthalpy (−103.5 kJ/mol) for bixbyite when no reduction occurs. Thus, it appears that the sample surfaces are passivized against reduction with ~2% total surface water coverage when that water remains on the surface for 24 h (or remains on the surface from the synthesis and lower-temperature heat treatment). Therefore, a water-free initial surface appears necessary to start the rapid reduction process when water is first introduced at room temperature.

For samples in which the reduction following water adsorption did occur, the extent of reduction, the shape of the isotherm, the coverage for full chemisorption (i.e., the total water content after which further doses produced only physisorbed water with an enthalpy of adsorption of −44 kJ/mol), and the enthalpy were all reproducible and did not depend on the dose size (see Table 2). Furthermore, the reduction process was reversible and the sample could be cycled (dehydration at 700 °C followed by water adsorption) at least three times with reproducible results. These observations suggest thermodynamic control of the process.

The initial state (wet versus dry) of nanoparticle surfaces influences the thermodynamic driving force for reduction. At 25 °C for bulk materials, for the reaction $Mn_2O_3 = 2/3\ Mn_3O_4 + 1/6\ O_2$, $\Delta H^o_{red} = 36.0$ kJ/mol calculated from standard thermodynamic data (5). At the nanoscale, this value is modified by terms arising from the difference in surface energies, as discussed by Birkner and Navrotsky (3). Assuming the same molar surface areas for Mn_2O_3 and 2/3 Mn_3O_4, this correction is then simply estimated as the product of molar surface area (SA) and the difference in surface energy (SE) of Mn_3O_4 and Mn_2O_3: $\Delta(\Delta H_{red}) = SA(SE(Mn_3O_4) - SE(Mn_2O_3))$. Using the surface area of 2941 m^2/mol for the particles in this study (Table 1), and values of SE from Birkner and Navrotsky (3), which are Mn_3O_4: SE (hydrous surface) = 0.96 J/m^2 and SE (anhydrous surface) = 1.62 J/m^2 and Mn_2O_3: SE(hydrous surface) = 1.29 J/m^2 and SE (anhydrous surface) = 1.77 J/m^2, one obtains $\Delta(\Delta H_{red}) = -0.44$ kJ/mol for anhydrous particles and −0.97 kJ/mol for hydrous particles. These calculations, although very approximate, clearly show that the driving force for reduction becomes less unfavorable for nanoparticles, with a significantly greater effect for hydrated particles. Thus, both size diminution and hydration favor hausmannite (lower surface energy phase) over bixbyite (higher surface energy phase).

Table 2. Comparison of Mn_2O_3 samples prepared for various water adsorption experiments using 700 °C procedure versus 350 °C procedure

Mn_2O_3	Water adsorption, 350 °C	Water adsorption, 700 °C	Water adsorption, one large dose, 700 °C	Water adsorption, two large doses, 700 °C	Water adsorption, three large doses, 700 °C
Phase (particle size, nm)	Mn_2O_3 (32.6)	85% Mn_2O_3 (28.7) and 15% Mn_3O_4 (25.6)	85% Mn_2O_3 (30.7) and 15% Mn_3O_4 (26.9)	85% Mn_2O_3 (31.3) and 15% Mn_3O_4 (25.9)	85% Mn_2O_3 (30.5) and 15% Mn_3O_4 (26.0)
Coverage, molecules H_2O/nm^2	4.8	4.7	4.9	5.1	4.7
Mn average oxidation state	3.00 ± 0.01	2.93 ± 0.01	2.93 ± 0.01	2.93 ± 0.01	2.93 ± 0.01
Preadsorption coverage *	2.30 E-2	2.06 E-4	2.06 E-4	2.06 E-4	2.06 E-4
First dose as preadsorbed,* mmol	1.17 E-4	1.00 E-06	CBD	CBD	CBD
Total water adsorbed, mmol, and doses accrued at coverage	2.15 E-2, 8 doses	2.31 E-2, 8 doses	1.51 E-2, 1 dose	1.48 E-2, 1 dose	1.47 E-2, 1 dose
Integral ΔH_{ads}, kJ/mol	−103.1 ± 0.9, −103.5†	−90.2 ± 0.9	CBD	CBD	CBD

CBD, cannot be determined.

*Preadsorption coverage is the computed number of molecules water per nm^2 surface per mole Mn_2O_3 evaluated using residual surface water taken from annealing experiments and specific surface area (see *SI Text*).

†Birkner and Navrotsky (3). CBD, because the point at which the sample achieves the full coverage value during the large dose water adsorption experiment is not well defined and cannot yield an integral enthalpy of chemisorption.

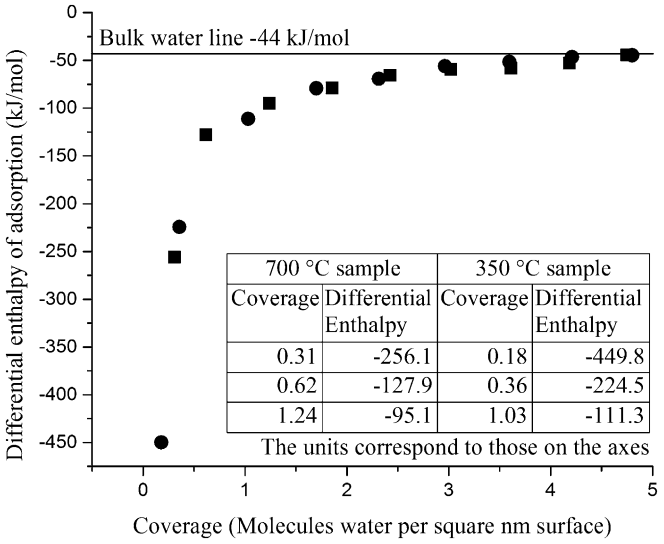

Fig. 3. Differential enthalpy of water adsorption as a function of water molecule coverage for Mn_2O_3 samples prepared with 350 °C (circles) and 700 °C (squares) pretreatment methods. (*Inset*) The table illustrates the more endothermic values for the 700 °C sample for the three initial doses, which leads to the less exothermic integral enthalpy.

For 15% reduction, we calculate an endothermic enthalpy contribution of $0.15(\Delta H^{o}_{red} + \Delta(\Delta H_{red}) = 5.3$ kJ/mol, which is significantly less than the value (12.9 ± 0.9 kJ/mol) obtained from the differences in water adsorption enthalpies. This difference probably reflects the approximate nature of the calculation using surface areas and surface energies, and the possible complexity of the redox process. Nevertheless, it confirms that the difference in measured water adsorption enthalpies reflects the energetics of reduction coupled with water adsorption.

It is notable that only 15% of the Mn_2O_3 is reduced, and that this fraction appears reproducible for several different water adsorption protocols on the same starting material. The polydispersity of particle size may be a critical factor. The smaller the Mn_2O_3 particle, the less endothermic is its enthalpy of reduction, as shown by the equations above. Since one does not know the oxygen fugacity in the water adsorption tube, one cannot calculate the free energy, and therefore the particle size, for reduction to become favorable. It is likely that only the smaller particles in the synthetic assemblage meet this threshold. In this scenario, the product of 85% Mn_2O_3 and 15% Mn_3O_4 would consist of a mixture of separate particles of bixbyite and hausmannite, with the Mn_3O_4 having smaller average particle size than the Mn_2O_3. Another possible scenario is that there may be somewhat larger particles with a shell of hausmannite covering a core of unreduced bixbyite. This could occur if the spinel shell were dense and coherent enough to hinder gas transport. Thus, the sample could consist of three kinds of particles, small ones that are totally reduced, core-shell particles of intermediate size, and large ones of unaltered bixbyite. Calculations of particle size from XRD (Scherrer equation) are not sensitive enough to provide such detail. Transmission electron microscopy might be useful but it could be complicated (perhaps even fatally) by the rapid redox and dehydration reactions that may occur under high vacuum and electron irradiation in transmission electron microscopy.

Passivation by water adsorption at 350 °C may also involve mainly the smaller particles of Mn_2O_3, perhaps explaining why a very low adsorbed water content appears effective. At that temperature, water adsorption may form an amorphous MnOOH layer without reduction, which may hinder gas transport. Moreover, leaving the water-treated sample for several months at room temperature caused it to further transform partially to MnOOH (a poorly crystalline layered phase), as observed previously for nanophase hausmannite samples (3, 6). This suggests that, although the observed water-induced redox equilibrium is reversible and represents local equilibrium, a state of lower free energy, the layered oxyhydroxide, can be attained with time. An analogous effect was seen previously (3), where reduction of nanophase MnO_2 produced an amorphous and, presumably, hydrated surface layer. Likewise, an amorphous Mn(IV) oxide layer may be present in amounts too small for easy characterization without the use of high energy source spectroscopy methods.

Discussion: Geochemical and Technological Implications

Hydration-induced mineral phase transformations that occur near room temperature could affect the properties of the material in technological applications as well as in geologic settings. Previously, we found that nanoparticle surface energy and hydration energy differences promote significant Gibbs free energy shifts in redox phase equilibria at the nanoscale (2). The spinel phase Mn_3O_4 (hausmannite) has a lower surface enthalpy than Mn_2O_3 (bixbyite), while the latter has a smaller surface energy than MnO_2 (pyrolusite) (3). Thus, the stability field of Mn_3O_4 is greatly extended at the nanoscale. We then focused on the energetics of nanosheets of calcium manganese oxide (CaMnO). We found that these layered phases are highly thermodynamically stable and have significantly lower surface energy than the binary manganese oxides Mn_3O_4, Mn_2O_3, and MnO_2 (7). The enthalpy of oxidation of CaMnO materials was independent of the average oxidation state and significantly less exothermic that the oxidation of Mn_2O_3 to MnO_2. We also suggested that the above factors are important in enhancing the catalytic activity of the layered CaMnO materials by facilitating adsorption/desorption and surface transport of water, ions, and electrons. In the present study, we extend this examination toward the influence of room-temperature chemisorption of water on anhydrous nanophase surfaces of Mn_2O_3, which resulted in reduction and the formation of a surface layer of Mn_3O_4. We do not know whether this reduction occurs by water oxidation or the direct release of oxygen from the solid phase. However, this reaction produces oxygen (Eq. **1**), regardless of the details of mechanism, and our thermodynamic calculations show it can indeed occur at a higher oxygen partial pressure (fugacity) at the nanoscale than in the bulk. Collectively, the phenomena observed in this and our earlier study (3) provide a facilitative redox environment mediated by water chemisorption and surface energy of nanoparticles. This behavior may be important for geochemistry and catalysis as illustrated below.

In common near-surface Earth environments, temperature–pressure–water fugacity fluctuations are generally not extreme enough to dehydrate nanoparticles. However, there are certain specialized environments on Earth and other planets where hydration-driven redox reactions could be important. For instance, manganese oxide coatings (rock varnish or patinas) are produced over long periods of time in thin layers on rock faces, stone monuments, and archeological artifacts, although most commonly found in a desert climate that alternates periods of aridity with sporadic mineral surface wetting (8). Changes in manganese oxide redox equilibria at these surfaces during such occasional "wet" periods may interact with the bacterial biogeochemical cycles suggested as important in the process of forming desert varnish (9). Bixbyite $[Mn,FeO_3]$ is found in the near-surface environment in cavities of rhyolite host rock (10) and hydrothermal or metamorphic deposits (11) along with hausmannite, where it serves as an important geothermometer for some ore deposits (11). We argue that the water-induced phenomenon of reduction of Mn_2O_3 nanoparticles requires an initially dry environment, partly to avoid MnOOH formation (*supra vide*). Thus, large swings in humidity, as in an arid environment (both

on the surface and in soils), would provide terrestrial settings where the phenomena we have observed could occur in nature. Our point is that such water-induced reactions can occur locally and on short time scales. Similar reactions may occur involving other pairs of mineral phases, e.g., Mn_2O_3–MnO_2 or Fe_3O_4–Fe_2O_3, making water-induced redox changes potentially general phenomena worthy of further study.

The surface of Mars currently has a very thin atmosphere, but the possibility of mineral surface hydration under Martian conditions was investigated in the laboratory (12, 13) and recently detected directly at Gale Crater, Mars (14). There are great diurnal temperature differences and sheltered basins with subsequent transient melting of ice (15–17) and craters where the atmospheric pressure is higher than average (18, 19). In addition, very high salt concentration in Martian soils (20–22) may contribute to melting of ice in addition to an increase mineral surface dehydration by lowering water activity. These conditions may set the stage for hydration-/dehydration-driven redox reactions, which may apply to iron oxides as well as manganese oxides. The salient point of the current study is that such reactions can occur rapidly and, therefore, the redox states detected on the surface of Mars may reflect contemporary as well as ancient conditions.

Surface water content may be mediated through competition by organic species, ranging from small molecules with carboxylic or phenolic groups to proteins generated by microorganisms (23–25). When such molecules chelate strongly, they may compete with water at the mineral–solution interface and thus may affect surface redox reactions and contribute to weathering processes, which in turn are critical for microbial activity (26–28) and manganese bioavailability (29). Such water-mediated coupling between organic and inorganic species may be important not only in contemporary environments but also in ancient ones, including prebiotic reactions on redox active nanoscale mineral surfaces leading to the origin and evolution of life (30). The coupling of redox and hydration reactions on nanoparticles may thus provide unique mechanisms for prebiotic or biological control of oxidation state.

These observations also suggest a possible mechanism of coupling surface redox reactions involving different metals. Formation of a low surface energy spinel surface layer coating of a stable metal oxide like Mn_3O_4 provides a surface active toward both electron transfer and the adsorption/desorption of water, inorganic ions, and other molecules. Hematite, Fe_2O_3, could readily undergo reduction to magnetite on such a surface, or magnetite could be oxidized to maghemite, the underlying spinel surface providing topotaxy. Madden and Hochella (31) have studied a related coupled redox surface reaction involving nanophase manganese oxides that form as a result of catalytic oxidation of aqueous manganese(II) on ferrihydrite surfaces. Metal oxide surfaces are able to accelerate Mn(II) oxidation by O_2. Examples are provided by hematite and manganese dioxide (32); lepidocrocite (33); goethite, lepidocrocite, and alumina (34); and colloidal hexagonal birnessite (35). The present study suggests that these reactions will be affected or perhaps even thermodynamically driven by both particle size and degree of hydration and that the equilibria can respond rapidly to changes in water availability.

Nanophase transition metal oxide particles are invoked in many actual and potential catalytic processes, e.g., carbon monoxide oxidation, organic synthesis by Fischer–Tropsch reactions, and desulfurization of exhaust gases (36, 37). In such processes, the preparation of the catalyst is critical to its function. Often such preparation involves a final "activation" step, wherein the catalyst is exposed for a controlled period to a temperature high enough to remove all or most surface water but not high enough to change its morphology and particle size (38, 39). The catalyst is then used at lower temperatures. These observations suggest that such an activated surface will undergo redox reactions upon initial contact with water, while a more hydrated surface will not. Many catalytic processes have some water present or produced during reaction, so such water-driven redox reaction may change the catalyst surface and perhaps aid catalysis by producing a material with mixed oxidation states. Continued hydration may prevent further redox activity and, as is often observed, "poison" the catalyst. Thus, the observations in this paper may pave the way to understanding the interaction of oxide catalyst surfaces with water and optimizing catalytic conditions.

In conclusion, the present work suggests a strong coupling between surface hydration and redox reactions on nanoscale manganese oxide (and likely other metal oxide) surfaces. Such coupling may influence the progress of (bio)geochemical, planetary, environmental, and technological processes.

Materials and Methods

Nanophase Mn_2O_3 was synthesized using a previously reported oxidative precipitation method (3). The synthesis details are in *SI Text*. All phases were analyzed using a Bruker AXS D8 Advance diffractometer (Cu Kα radiation, 1.540596 Å) operated at 45 kV and 40 mA. The X-ray powder patterns were collected at room temperature (25 °C) using a step size of 0.02 °2θ and 10 s dwell time. Peak profiles were fitted with a pseudo-Voigt function. International Center for Diffraction Data (ICDD) reference patterns were used in conjunction with analysis performed with Jade software (version 6.11, 2002; Materials Data Inc.) to evaluate the phases or phase mixtures present, their amounts, lattice parameters, and estimated crystallite sizes using the Scherrer equation (40, 41). The identified Mn_2O_3 corresponded to ICDD file number 41-1442 (42) and Mn_3O_4 to ICDD file number 80-0382 (43). Specific surface area was measured by N_2 adsorption at −196 °C using a five-point Brunauer–Emmett–Teller (BET) technique on a Micromeritics ASAP 2020 (44). The samples were heated to 700 °C at 10 °C/min under a flow of argon (75 mL/min) in platinum crucibles using the Setaram Labsys Evo instrument and associated Calisto software. The TGA data were corrected for buoyancy by running an empty crucible. H_2O content was determined from the weight difference (obtained on a microbalance for highest accuracy) before and after annealing the samples overnight at 700 °C. Experiments used controlled heating to observe changes in the amount of water, phases present, and oxidation states in the samples, for which the methods used are detailed in *SI Text*. Mn average oxidation state was measured by iodometric titration (45). The method titrates iodine produced by the reaction of iodide with dissolved manganese and can be performed at room temperature. The specific details of the titration of Mn(III and IV) oxidation state and calculations are described in detail elsewhere (7). The enthalpy of water adsorption was measured by calorimetry at room temperature using a Calvet microcalorimeter, coupled with a Micromeritics ASAP 2020 analysis system as described previously (4). The percent surface coverage relates the nanophase sample surface area to the area that would be covered by water based on water molecule size (10.8 A^2) (46). Some water can exist in pores/boundaries produced by nanoparticle aggregation, although pore water behavior cannot be distinguished from that of surface water. However, the degree of aggregation is small, since the particle size obtained by X-ray and BET agree.

Details of methodology, figures for X-ray powder patterns, and additional details of characterization techniques—XRD, BET, TGA, controlled heating and cooling experiments, water adsorption calorimetry, and preadsorbed water calculation—are provided in *SI Text*.

ACKNOWLEDGMENTS. This research received support from the U.S. Department of Energy, Grant DE-FG02-97ER14749.

1. Navrotsky A (2009) Energetics of oxide nanoparticles. *Int J Quantum Chem* 109(12): 2648–2657.
2. Navrotsky A, Ma C, Lilova K, Birkner N (2010) Nanophase transition metal oxides show large thermodynamically driven shifts in oxidation–reduction equilibria. *Science* 330(6001):199–201.
3. Birkner N, Navrotsky A (2012) Thermodynamics of manganese oxides: Effects of particle size and hydration on oxidation-reduction equilibria among hausmannite, bixbyite, and pyrolusite. *Am Mineral* 97(8-9):1291–1298.
4. Ushakov SV, Navrotsky A (2005) Direct measurements of water adsorption enthalpy on hafnia and zirconia. *Appl Phys Lett* 87(16):164103.

5. Robie RA, Hemingway BS (1995) Thermodynamic properties of minerals and related substances at 298.15 K and 1 bar (105 Pascals) pressure and at higher temperatures. *US Geol Surv Bull* 1452:1–456.
6. Kirillov SA, et al. (2009) Oxidation of synthetic hausmannite (Mn_3O_4) to manganite (MnOOH). *J Mol Struct* 928(1-3):89–94.
7. Birkner N, et al. (2013) Energetic basis of catalytic activity of layered nanophase calcium manganese oxides for water oxidation. *Proc Natl Acad Sci USA* 110(22): 8801–8806.
8. DiGregorio BE (2002) Rock varnish as a habitat for extant life on Mars. *Instruments, Methods, and Missions for Astrobiology IV*, eds Hoover RB, Levin GV, Paepe RR, Rozanov AY (Int Soc Opt Eng, Bellingham, WA), pp 120–130.
9. Perry RS, Kolb VM (2004) Biological and organic constituents of desert varnish: Review and new hypotheses. *Instruments, Methods, and Missions for Astrobiology VII*, eds. Hoover RB, Rozanov AY (Int Soc Opt Eng, Bellingham, WA), pp 202–217.
10. Christiansen EH, Bikun JV, Sheridan MF, Burt DM (1984) Geochemical evolution of topaz rhyolites from the Thomas Range and Spor Mountain, Utah. *Am Mineral* 69(3-4):223–236.
11. Mason B (1944) The system Fe_2O_3–Mn_2O_3: Some comments on the names bixbyite, sitaparite, and partridgeite. *Am Mineral* 29(1-2):66–69.
12. Jänchen J, Bish DL, Möhlmann DTF, Stach H (2006) Investigation of the water sorption properties of Mars-relevant micro- and mesoporous minerals. *Icarus* 180(2):353–358.
13. Bish DL, Carey W, Vaniman DT, Chipera SJ (2003) Stability of hydrous minerals on the martian surface. *Icarus* 164(1):96–103.
14. Meslin PY, et al.; MSL Science Team (2013) Soil diversity and hydration as observed by ChemCam at Gale crater, Mars. *Science* 341(6153):1238670.
15. Hecht MH (2002) Metastability of liquid water on Mars. *Icarus* 156(2):373–386.
16. Lobitz B, Wood BL, Averner MM, McKay CP (2001) Use of spacecraft data to derive regions on Mars where liquid water would be stable. *Proc Natl Acad Sci USA* 98(5): 2132–2137.
17. Savijärvi H (1995) Mars boundary layer modeling: Diurnal moisture cycle and soil properties at the Viking Lander 1 Site. *Icarus* 117(1):120–127.
18. Heldmann JL, et al. (2005) Formation of Martian gullies by the action of liquid water flowing under current Martian environmental conditions. *J Geophys Res* 110:E05004, 10.1029/2004JE002261.
19. Farmer CB, Doms PE (1979) Global and seasonal variations of water vapor on Mars and the implications for permafrost. *J Geophys Res* 84(B6):2881–2888.
20. Möhlmann D, Thomsen K (2011) Properties of cryobrines on Mars. *Icarus* 212(1): 123–130.
21. Rennó N, et al. (2009) Possible physical and thermodynamic evidence for liquid water at the Phoenix landing site. *J Geophys Res* 114:E00E03, 10.1029/2009JE003362.
22. Sears DWG, Chittenden JD (2005) On laboratory simulation and the temperature dependence of the evaporation rate of brines on Mars. *Geophys Res Lett* 32:L23203, 10.1029/2005GL024154.
23. Duckworth OW, Bargar JR, Sposito G (2009) Coupled biogeochemical cycling of iron and manganese as mediated by microbial siderophores. *Biometals* 22(4):605–613.
24. Stumm W, Morgan JJ (1996) *Aquatic Chemistry: Chemical Equilibria and Rates in Natural Waters* (Wiley, New York), pp 648–651 and 872–934.
25. Sposito G (1989) *The Chemistry of Soils* (Oxford Univ Press, New York), pp 42–65.
26. Brown GE, Jr., Calas G (2013) Mineral-aqueous solution interfaces and their impact on the environment. *Geochem Perspect* 1(4-5):483–742.
27. Tebo BM, Geszvain K, Lee SW (2010) The molecular geomicrobiology of bacterial manganese(II) oxidation. *Geomicrobiology: Molecular and Environmental Perspective*, eds Barton BL, Mandl M, Loy A (Springer, Dordrecht, The Netherlands), pp 285–308.
28. Tebo BM, et al. (2004) Biogenic manganese oxides: Properties and mechanisms of formation. *Annu Rev Earth Planet Sci* 32:287–328.
29. Stumm W, Morgan JJ (1996) *Aquatic Chemistry: Chemical Equilibria and Rates in Natural Waters* (Wiley, New York), 3rd Ed, pp 632–643.
30. Hazen RM, Sverjensky DA (2010) Mineral surfaces, geochemical complexities, and the origins of life. *Cold Spring Harb Perspect Biol* 2(5):a002162.
31. Madden AS, Hochella MF, Jr. (2005) A test of geochemical reactivity as a function of mineral size: Manganese oxidation promoted by hematite nanoparticles. *Geochim Cosmochim Acta* 69(2):389–398.
32. Wilson DE (1980) Surface and complexation effects on the rate of Mn(II) oxidation in natural waters. *Geochim Cosmochim Acta* 44(9):1311–1317.
33. Sung W, Morgan JJ (1981) Oxidative removal of Mn(II) from solution catalyzed by γ-FeOOH surface. *Geochim Cosmochim Acta* 45(12):2377–2383.
34. Davies SHR, Morgan JJ (1989) Manganese(II) oxidation kinetics on metal oxide surfaces. *J Colloid Interface Sci* 129(1):63–77.
35. Learman DR, Voelker BM, Vazquez-Rodriguez AI, Hansel CM (2011) Formation of manganese oxides by bacterially generated superoxide. *Nat Geosci* 4(2):95–98.
36. Slimane RB (1994) Desulfurization of hot coal-derived fuel gases with manganese-based regenerable sorbents. PhD dissertation (Univ of Minnesota, Minneapolis).
37. Soerawidfaja TH (1985) Steam-regenerative removal of H2S at high temperatures using metal oxide on alumina acceptors. PhD dissertation (Delft University Press, Delft, The Netherlands).
38. Slimane RB, Hepworth MT (1994) Desulfurization of hot coal-derived fuel gases with manganese-based regenerable sorbents. 2. Regeneration and multicycle tests. *Energy Fuels* 8(6):1184–1191.
39. Wakker JP, Gerritsen AW, Moulijn JA (1993) High temperature H_2S and COS removal with MnO and FeO on γ-Al_2O_3 acceptors. *Ind Eng Chem Res* 32(1):139–149.
40. Scherrer P (1918) Bestimmung der Grösse und der inneren Struktur von Kolloidteilchen mittels Röntgenstrahlen. *Nachr Ges Wiss Göttingen* 26(2):98–100.
41. Patterson AL (1939) The Scherrer formula for X-ray particle size determination. *Phys Rev* 56(10):978–982.
42. Geller S (1971) Structures of alpha-Mn_2O_3, $(Mn_{0.983}Fe_{0.017})_2O_3$ and $(Mn_{0.37}Fe_{0.63})_2O_3$ and relation to magnetic ordering. *Acta Crystallogr B* 27(4):821–828.
43. Jarosch D (1987) Crystal structure refinement and reflectance measurements of hausmannite. *Mineral Petrol* 37:15–23.
44. Brunauer S, Emmett PH, Teller E (1938) Adsorption of gases in multimolecular layers. *J Am Chem Soc* 60(2):309–319.
45. Murray JW, Balistrieri LS, Paul B (1984) The oxidation state of manganese in marine sediments and ferromanganese nodules. *Geochim Cosmochim Acta* 48(6):1237–1247.
46. McClellan AL, Harnsberger HF (1967) Cross-sectional areas of molecules adsorbed on solid surfaces. *J Colloid Interface Sci* 23(4):577–599.